nature plants

ARTICLES

https://doi.org/10.1038/s41477-019-0525-6

Structural and functional insights into the tetrameric photosystem I from heterocyst-forming cyanobacteria

Lvqin Zheng[1,5], Yanbing Li[2,5], Xiying Li[2,5], Qinglu Zhong[3], Ningning Li[1], Kun Zhang[2], Yuebin Zhang[3], Huiying Chu[3], Chengying Ma[1], Guohui Li[3*], Jindong Zhao[2,4*] and Ning Gao[1*]

Two large protein-cofactor complexes, photosystem I and photosystem II, are the central components of photosynthesis in the thylakoid membranes. Here, we report the 2.37-Å structure of a tetrameric photosystem I complex from a heterocyst-forming cyanobacterium *Anabaena* sp. PCC 7120. Four photosystem I monomers, organized in a dimer of dimer, form two distinct interfaces that are largely mediated by specifically orientated polar lipids, such as sulfoquinovosyl diacylglycerol. The structure depicts a more closely connected network of chlorophylls across monomer interfaces than those seen in trimeric PSI from thermophilic cyanobacteria, possibly allowing a more efficient energy transfer between monomers. Our physiological data also revealed a functional link of photosystem I oligomerization to cyclic electron flow and thylakoid membrane organization.

Oxygenic photosynthesis plays an important role in converting solar energy into chemical energy. Two large protein complexes, photosystem I (PSI) and photosystem II (PSII), embedded in the thylakoid membranes of plants and cyanobacteria, are responsible for the important initial steps of the light-induced electron transport[1]. In linear electron flow, PSII, cytochrome (Cyt) b_6f complex and PSI act sequentially to transfer electrons from water to ferredoxin/flavodoxin to reduce nicotinamide adenine dinucleotide phosphate ($NADP^+$) and to generate a proton gradient across the membranes for ATP biosynthesis. PSI also has a function in cyclic electron flow (CEF) to produce ATP without accumulation of NADPH (the reduced form of $NADP^+$)[1]. Both PSI and PSII are highly conserved and exist in different oligomeric states in photosynthetic membranes of different species. Generally, PSI acts as a monomer in chloroplasts of land plants or as an oligomer in most cyanobacteria, and PSII acts exclusively as a dimer[2–5]. Over the years, structures of cyanobacterial PSI complexes and the plant supercomplexes formed between PSI and light-harvesting complexes have been well studied, and the general principles governing subunit organization and energy transfer have been researched in considerable detail[4,6–14].

The crystal structure of PSI trimers from *Thermosynechococcus elongatus*[7] and *Synechocystis* sp. PCC 6803 (*Synechocystis* 6803)[13] and also biochemical data[15,16] revealed that one protein subunit of PSI, PsaL, is primarily responsible for the trimerization of PSI complexes. PsaH, which is not found in cyanobacteria, binds to PsaL in plants and prevents the oligomerization of PSI[17–19]. However, except for a low-resolution structure[20], much less is known about the structure and unique function of tetrameric PSI in the heterocyst-forming cyanobacteria, such as *Chroococcidiopsis* sp.[21] and *Cyanophora paradoxa*[22].

In this study, we selected a filamentous cyanobacterium *Anabeana* sp. PCC 7120 (*Anabaena* 7120) to study the structure and functions of tetrameric PSI. *Anabaena* 7120 can form specialized cells called heterocysts for nitrogen fixation in the absence of combined nitrogen[23]. We took advantage of the fact that the only active photosystem in heterocysts is PSI performing CEF for ATP biosynthesis[24]. This provides an ideal model for us to focus exclusively on the functions of PSI.

Overall structure of the tetrameric PSI

To understand the organization of tetrameric PSI, we purified PSI tetramers from *Anabaena* 7120 using sucrose-density gradient centrifugation (Supplementary Fig. 1). To mitigate the sample dissociation during cryo-grid prepration, GraFix[25] was used to stabilize the PSI tetramer. Subsequent cryogenic electron microscopy (cryo-EM) analysis generated a final density map at an overall resolution of 2.37 Å (Supplementary Fig. 2). All 12 subunits of PSI (PsaA–PsaF, PsaI–PsaM and PsaX) could be identified and modelled (Fig. 1). For each monomer, we also modelled 123 cofactors, including 95 chlorophylls, two phylloquinones, three Fe_4S_4 iron–sulfur clusters and 23 carotenoids (Supplementary Fig. 3). The tetramer exhibits a rhomboidal shape (250×170 Å^2), comprising a dimer of dimer (Fig. 1a). The components of electron transfer chain of individual PSI monomers, from P700 (the closely associated pair of chlorophylls, which are the first observable oxidized species in the electron transfer, also known as the 'special pair') to the iron–sulfur cluster F_B, and the distances between them are nearly identical to those reported for the trimeric PSI complex[7]. In contrast to the trimeric form of PSI, which is tightly packed and perfectly symmetrical[7,26,27], the tetrameric PSI is rather loosely assembled and contains a central cavity (75×35 Å^2), which is presumably filled with lipids in the membrane environment.

Compared with the trimeric PSI, the four monomers in the PSI tetramer contain two conformers, and therefore two distinct interfaces (interfaces I and II) exist in a tetrameric PSI. The two

[1]State Key Laboratory of Membrane Biology, Peking-Tsinghua Center for Life Sciences, Academy for Advanced Interdisciplinary Studies, School of Life Sciences, Peking University, Beijing, China. [2]State Key Laboratory of Protein and Plant Genetic Engineering, School of Life Sciences, Peking University, Beijing, China. [3]State Key Laboratory of Molecular Reaction Dynamics, Dalian Institute of Chemical Physics, Chinese Academy of Sciences, Dalian, China. [4]Chinese Academy of Sciences Key Laboratory of Phycological Research, Institute of Hydrobiology, Chinese Academy of Sciences, Wuhan, Hubei, China. [5]These authors contributed equally: Lvqin Zheng, Yanbing Li, Xiying Li. *e-mail: ghli@dicp.ac.cn; jzhao@pku.edu.cn; gaon@pku.edu.cn

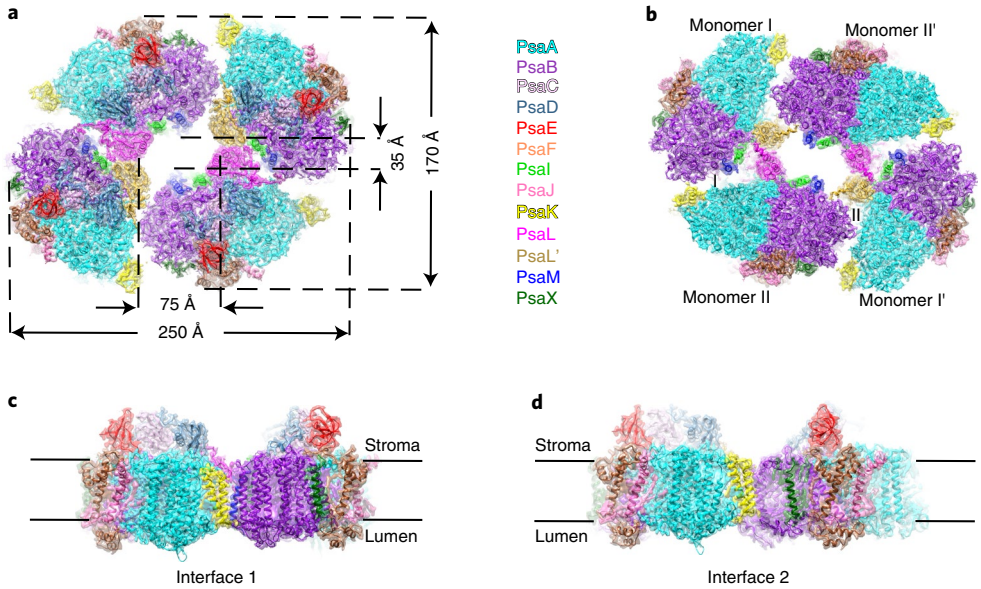

Fig. 1 | Cryo-EM structure of the tetrameric PSI complex. a, The tetrameric PSI complex viewed from the stromal side. The cryo-EM density map is shown in transparent surface representation, superimposed with the atomic model. Each subunit is colour coded as indicated. **b**, View from the luminal side. Interfaces I and II are formed by different sets of PSI subunits. **c**,**d**, Side view of interface I (**c**) and interface II (**d**) along the membrane plane.

conformers are nearly identical and the root mean square deviation (RMSD) between two conformers is only 0.19 Å. Interface I is generally similar to the one seen in the PSI trimer[7], but one monomer is seen to have both a lateral and rotational shift (Supplementary Fig. 4a–d). Subunits close to the interface I include PsaA, PsaL and PsaK from one monomer, and PsaB', PsaI', PsaL' and PsaM' from an adjacent monomer (Fig. 2a). Interface II is formed by the same two sides of the two neighbouring monomers; however, compared to interface I, one monomer is seen to undergo a very large rotation (Fig. 2d and Supplementary Fig. 4e–h). A different set of subunits and different surfaces are therefore used for interface II and, due to the rotation, PsaI and PsaM are no longer in interface II.

The organization of the tetramer suggests that its assembly on the membrane has probably gone through an intermediate as a dimer. To test this hypothesis, we performed in silico assembly of the tetramer from four monomers in the lipid environment using coarse-grained molecular dynamics (MD) simulation. By measuring the time-course distance changes between adjacent monomers during assembly, it was shown that interface I always forms first (Supplementary Fig. 5). Consistently, three-dimensaional (3D) classification revealed a PSI dimer (Supplementary Fig. 2), probably resulting from cryo-preparation induced tetramer dissociation. This dimer consists of two monomers through interface I. Together, these data indicate the presence of a dimer intermediate during the assembly of a tetramer from monomers in the lipid environment.

Intermonomer interactions mediated by PSI subunits

In the PSI trimer, PsaL plays a vital role in organizing the three monomers into a tightly packed complex because PsaL oligomerizes into a homo-trimer and forms the three-fold axis of the complex[7]. Deletion of the *psaL* gene abolished the formation of PSI trimers in cyanobacterium *Synechocystis* 6803 (refs. [15,16]). This prompted us to examine the intersubunit interactions that are crucial for the formation of tetramer.

At interface I, a tight hydrophobic packing is seen between the transmembrane helices of two adjacent PsaL subunits (Supplementary Fig. 6), as in the PSI trimer[7,13]. In addition, two polar contact sites between two monomers were also found. The first (2.6 Å) is between Arg85 of PsaK from one monomer and Ser214 of PsaB' from the other monomer (Fig. 2a,b): the side chain of Arg85 is able to form a hydrogen bond with the carbonyl oxygen of Ser214. The second involves two PsaL subunits in interface I (Fig. 2c): two residues of PsaL, Gly56 and Thr58 in a loop close to the stromal side form hydrogen bonds with two residues in a C-terminal helix of PsaL', Asn140 (2.4 Å) and Asn141 (2.8 Å), respectively. Notably, Gly56 is invariant and Thr58 is highly conserved among all cyanobacteria, whereas Asn140 and Asn141 are only conserved in heterocyst-forming species.

For interface II, only three protein–protein contact sites were identified (Fig. 2d). The first one also uses Arg85 of PsaK', but the side chain is pointing towards a different residue (3.9 Å) of PsaB, Tyr493 near the C-terminus (Fig. 2e). The second contact site is formed between the two largest subunits of PSI: PsaA' and PsaB. The carbonyl oxygen of Phe226 and the side chain of Thr227 of PsaB interact with the side chains of Trp486 (2.5 Å) and Asn489 (3.0 Å) of PsaA', respectively (Fig. 2f). The last contact site involves the C-terminal Gly172 of PsaL' and a loop residue His206 of PsaB, capable of forming a pair of hydrogen bonds through the carboxyl group of the terminal Gly172 (Fig. 2g). The three contact sites of interface II all lie at the luminal side.

The participation of PsaL in both interfaces of the tetramer predicts a key role of PsaL in tetramer formation. As expected, an *Anabaena* 7120 strain in which the *psaL* gene was inactivated (ΔpsaL) lost the ability to form the PSI dimer and tetramer and could only produce monomeric PSI (Supplementary Figs. 1 and 7). Complementation of ΔpsaL with a full copy of wild-type (WT) *psaL* gene from *Anabaena* 7120 led to the formation of the PSI tetramer (Supplementary Fig. 7a). Phylogenetic analysis of cyanobacterial PsaL sequences groups PsaL proteins from all heterocystous cyanobacteria together in Clad-III[21]. The PsaL sequences are highly conserved but, in general, contain three variable regions: the N-terminal extension, a middle loop between the second and the third transmembrane helices, and the C-terminal extension[21] (Supplementary Fig. 7c). To test if a *psaL* gene in Clad-II (mostly PSI trimer group) could complement ΔpsaL and lead to the formation of trimer PSI, the *psaL* gene from *Synechococcus* 7002 was transformed into ΔpsaL. The result (Supplementary Fig. 7b) showed that although the complementation was incomplete and many monomeric PSI particles were observed with negative staining EM, some trimeric

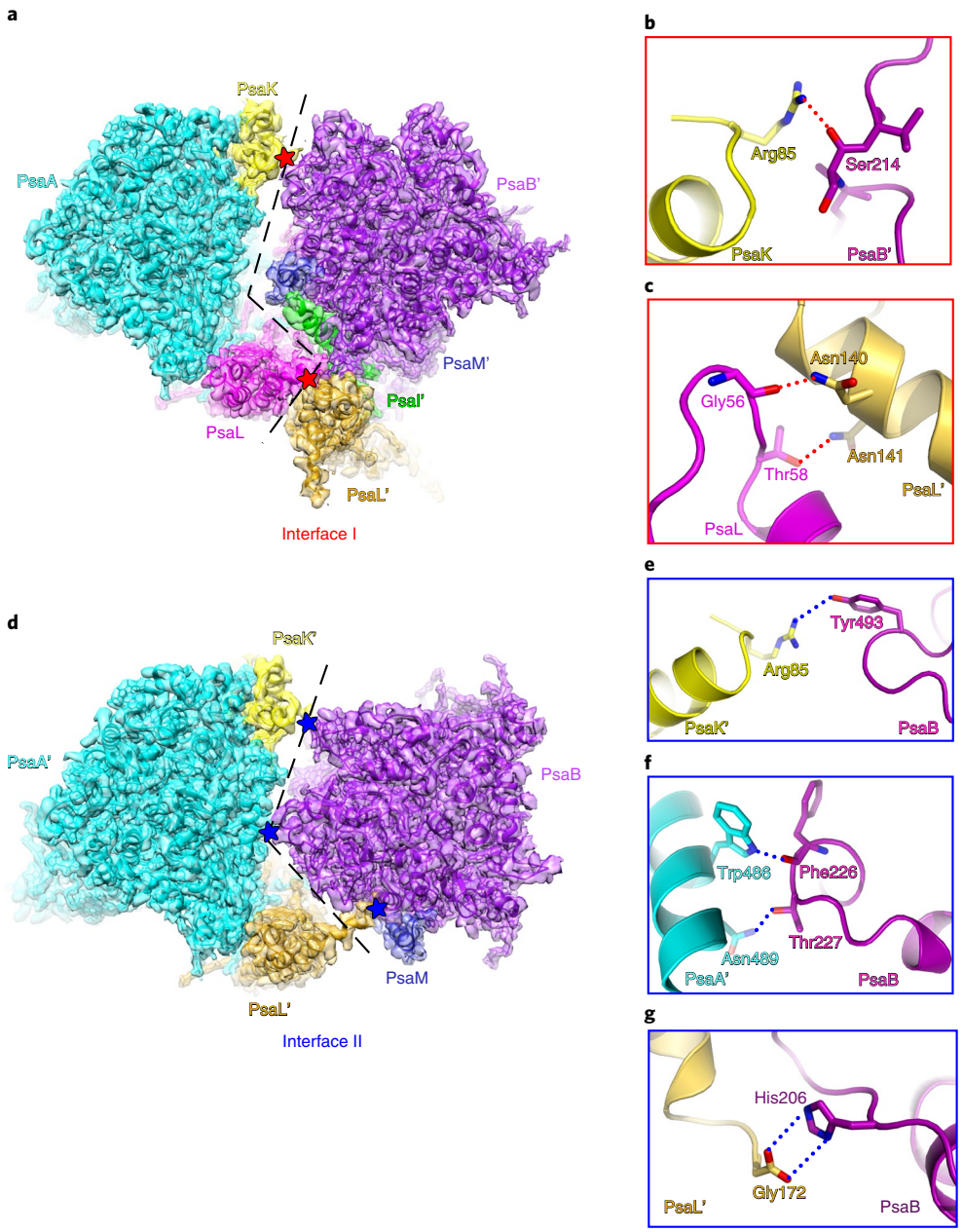

Fig. 2 | Intermonomer interactions mediated by PSI subunits. a, Subunits arrangement at interface I. Each subunit is colour coded as in Fig. 1. The boundary between two monomers are indicated by black dashed lines. Two protein–protein contact sites are labelled with red stars. **b**, Magnified view of the protein–protein interaction between PsaK and PsaB' in **a**. Possible hydrogen bonds are shown as red dashed lines. **c**, Magnified view of the protein–protein interaction between PsaL and PsaL' in **a**. **d**, Subunits arrangement at interface II. Three protein–protein contact sites are labelled with blue stars. **e–g**, Magnified view of protein–protein interactions at interface II (in **d**) between: Psak' and PsaB (**e**), PsaA' and PsaB (**f**), and PsaL' and PsaB (**g**). Possible hydrogen bonds are shown as blue dashed lines.

PSI particles could be seen, suggesting that PsaL plays a key role in determining the oligomeric state of PSI in cyanobacteria[21]. Specific residues of PsaL (most likely in the variable regions) are probably the primary determinant of the PSI oligomeric state.

Lipid molecules in the PSI tetramer

Four types of lipids, phosphatidyl glycerol (PG), monogalactosyldiacyl glycerol (MGDG), digalactosyldiacyl glycerol (DGDG) and sulfoquinovosyldiacyl glycerol (SQDG), have been previously identified in thylakoid membranes, and a variety of functions have been suggested, such as trimerization, light protection, biosynthesis and activity regulation of PSI[28–31].

In the PSI tetramer, a large number of bifurcated or trifurcated density rods could be found in the density map, and some could be fully modelled (Supplementary Figs. 3d–f and 5f–h). In a PSI dimer, we could model 13 lipid molecules of three types, including six PG, three MGDG and four SQDG (Fig. 3a). One interesting observation is that their head groups are all pointing towards the stromal side. Although no SQDG was identified in the PSI trimeric structure from *T. elongatus*[7], seven unsymmetrically distributed SQDG molecules were reported in the PSI trimer from *Synechocystis* 6803 (ref. [13]). In contrast, we found eight SQDG in the PSI tetramer, only one of which (position 3 in Fig. 3a) is in a nearly identical position in the *Synechocystis* PSI trimer. In the tetramer, four SQDG are located

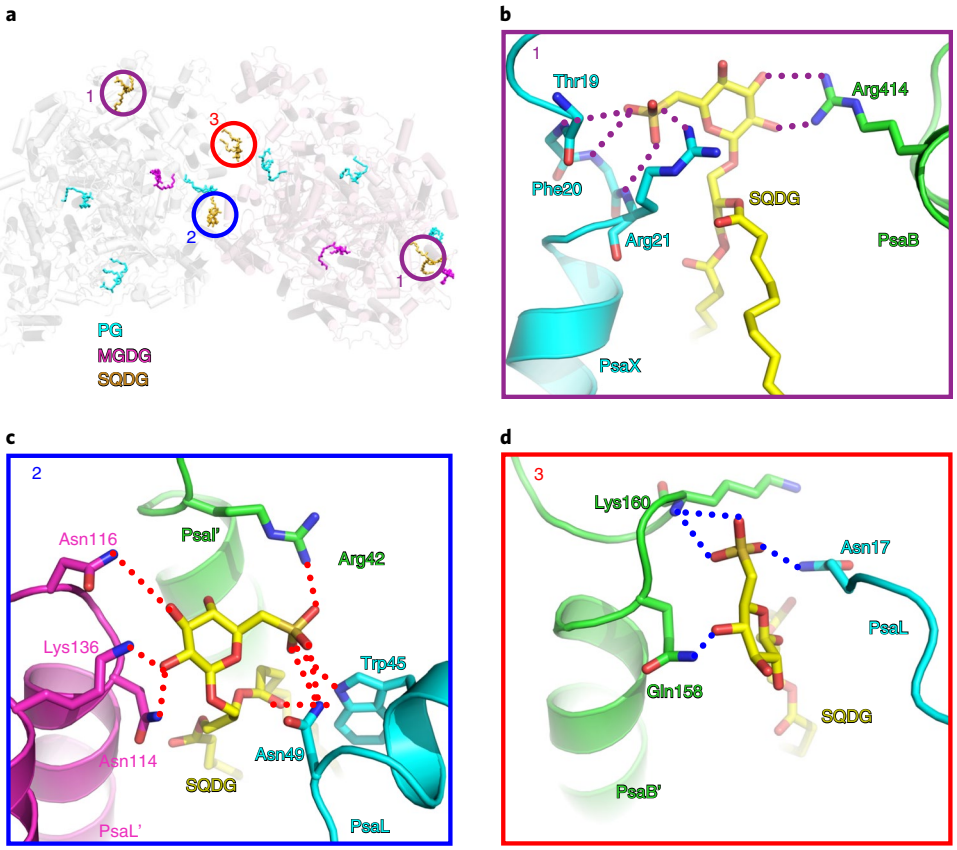

Fig. 3 | Lipid–protein interactions in the tetramer. a, Lipid distribution in a dimer. Two SQDGs located within two monomers are marked with purple circles (position 1). Two SQDGs located between two monomers marked as blue and red circles (positions 2 and 3, respectively). **b**, An SQDG connects PsaX to PsaB within a monomer (position 1 in **a**). Hydrogen bonds are shown as purple dotted lines. **c**,**d**, Two SQDGs mediate intermonomer interactions at interface I (positions 2 (**c**) and 3 (**d**) in **a**). Hydrogen bonds are shown as red and blue dotted lines, respecitvely.

between PsaB and PsaX of each monomer, occupying the equivalent position of a PG in the PSI trimer[7,13]. These four SQDG play a role in the assembly and stabilization of PsaX on a PSI monomer (Fig. 3b). The side chain of Arg414 of PsaB 'grabs' this SQDG through a pair of hydrogen bonds with the head group (2.4 Å, 3.4 Å). The sulfate group of this SQDG is embedded into the pocket formed by an N-terminal helix of PsaX, and extensive hydrogen bonds could form between the sulfate group and three main chain nitrogens of PsaX, Thr19 (3.5 Å), Phe20 (3.2 Å) and Arg21 (3.2 Å), and the side chain of Arg21 (2.7 Å).

The rest of SQDG in the PSI tetramer in interface I is capable of forming extensive hydrogen bonds with surrounding residues from the two monomers (Fig. 3c,d), manifesting an apparent role in mediating intermonomer interactions. The first SQDG is squeezed between three subunits: two PsaL and one PsaI. Side chains of Asn114 (2.7 Å), Asn 116 (3.8 Å) and Lys136 (2.8 Å) from PsaL', Trp45 (3.3 Å) and Asn49 (3.0 Å) from PsaL and Arg42 (3.2 Å) from the C-terminus of PsaI' are able to form a hydrogen bond network with the polar group of SQDG (Fig. 3c). Similarly, the other SQDG sits between PsaL and PsaB', and again through a hydrogen bond network to bridge the N terminus of PsaL (Asn17, 2.9 Å) and PsaB' (Gln158, 2.3 Å; Lys160, 2.9 Å) (Fig. 3d).

Our structure shows that lipids play specific role not only in the biogenesis (assembly) of PSI monomers to stabilize subunit interactions within a monomer, but also in the organization of monomers into oligomers in the tetrameric PSI. The distinct distribution of lipids within the PSI tetramer and trimer indicate that the regulation of lipid biosynthesis may influence the oligomeric state of PSI.

Lipids drive the assembly of the PSI tetramer

Given the presence of a large amount of lipids in the monomer interface, we set out to investigate the role of lipids in the assembly of the tetrameric PSI using MD simulation. A series of enhanced sampling MD simulations were performed to explore the assembly process of tetrameric PSI complex from four monomers in the lipid bilayer. In the trajectories of tetramer formation, relative changes of lipid composition within the complex could be analysed, and interestingly, a two-fold enrichment of MGDG in the central hole was found (Supplementary Fig. 5d). Next, we calculated the time-course of the potential energy contributed by PSI–PSI and lipid–PSI interactions. As expected, van der Waals interactions play a major role in the assembly process, and the contribution from van der Waals interactions between lipids and PSI is about 50-fold higher than the interactions among PSI monomers. Notably, when the potential energy is further fractioned into lipid classes, the largest contribution is from SQDG and MGDG (Fig. 4). These results suggest that the establishment of specific lipid interactions within the tetramer is probably the driving force for the tetramer assembly. In addition, the enrichment of specific lipids in the central hole suggests that lipid partition might be another factor in regulating the PSI biogenesis.

Chlorophyll network and energy transfer pathways

A total of 380 chlorophyll molecules were clearly resolved in a tetrameric PSI and were modelled with high accuracy (Supplementary Fig. 3). They form an interconnected network that reflects the complexity of energy transfer between chlorophylls in the PSI (Supplementary Fig. 8a). The distinct organization of the PSI tetramer allows us to examine

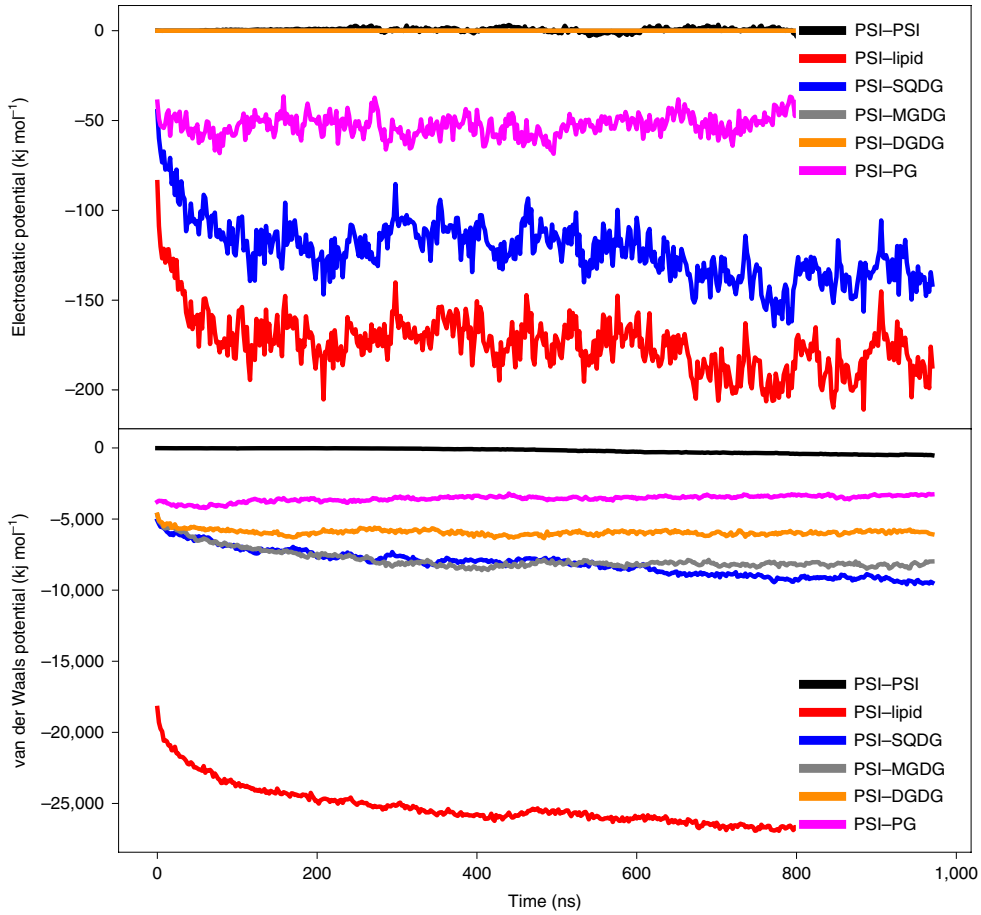

Fig. 4 | Time-course of the nonbonded interactions during the in silico assembly of PSI tetramer from monomers. The electrostatic and van der Waals interactions between PSI monomers and lipids are shown in the upper and lower panels, respectively. For both panels, the interactions between two adjacent PSI monomers are coloured in black, and the interactions between four PSI monomers and all lipids are coloured in red. The interactions between PSI monomers and each class of lipids, SQDG, MGDG, DGDG and PG are coloured in blue, grey, orange and magenta, respectively. The simulation was performed eight times independently and similar results were obtained.

possible energy transfer pathways that are absent in the PSI trimer. In general, chlorophyll network close to interface I is similar to that in the PSI trimers. Specifically, the excitation energy could be transferred from chlorophyll (Chl) *a*1801 and Chl *a*1121 to Chl *a*1208', with a magnesium–magnesium (Mg–Mg) distance of 18.9 Å and 20.8 Å, respectively, at the stromal side. The *a*1401–*a*1212' is the closest interfacial chlorophyll pair at the luminal side, with a Mg–Mg distance of 20.1 Å (Supplementary Fig. 8b).

We found that Mg–Mg distances between interfacial chlorophyll pairs are much shorter in the unique interface II, suggesting the presence of possibly faster and more efficient pathways in this interface. As shown in Supplementary Fig. 8a, a highly branched energy transfer network could possibly form due to a higher density of chlorophylls in interface II. At the stromal side, seven chlorophylls could form six energy transfer pairs (Supplementary Fig. 8c), with the shortest one at 15.2 Å between Chl *a*1801' and Chl *a*1217. Chl *a*1801' may also transfer the energy to another two chlorophylls (Chl *a*1209, 19.7 Å; Chl *a*1218, 16.9 Å). Furthermore, Chl *a*1501' serves as an alternative stromal-side energy transfer pathway to Chl *a*1208 (Mg–Mg distance 16.2 Å) and Chl *a*1209 (Mg–Mg distance 20.7 Å). Chl *a*1121' is also in close contact with Chl *a*1218, with a Mg–Mg distance of 17.8 Å. In contrast, at the luminal side of interface II, there are three relatively isolated chlorophyll pairs (Supplementary Fig. 8d): Chl *a*1233–*a*1401', Chl *a*1213–*a*1134' and Chl *a*1212 and Chl *a*1503', with Mg–Mg distances at 19.2 Å, 18.5 Å and 20.6 Å, respectively.

In summary, the efficiency of the energy transfer between monomers could possibly be higher in the tetramer than in the trimer due to the presence of a larger number of closely paired chlorophylls in the unique interface II in the tetramer.

Physiological role of PsaL in cyclic electron flow

We examined the possible cellular defects in the ΔpsaL strain because the deletion of PsaL prevented the formation of tetramers. First, we found that the overall PSI content was not altered in ΔpsaL as the levels of PSII and PSI in the mutant were comparable to that of the WT cells based on fluorescence emission spectra excited with 440 nm at 77 Kelvin (K) (Supplementary Fig. 9a). Second, we tested the energy transfer between phycobilisome (PBS) and PSI by measuring the 77 K fluorescence spectra excited with PBS-absorbing light at 590 nm (Supplementary Fig. 9b–d). The data showed that the allophycocyanin-B alpha subunit (ApcD)-mediated state transitions in ΔpsaL were not impaired as in other cyanobacteria[32,33]. It was noteworthy that the PSI emission of a mutant *Anabaena* 7120 (strain ΔcpcG3) lacking the *cpcL* gene[34] was lower than that of WT when excited at 590 nm, suggesting that CpcL–PBS is an important energy source for PSI in *Anabaena* 7120. These results are in agreement with the previous report that CpcL–PBS is associated with PSI[35] and they indicate that monomeric PSI in ΔpsaL could still receive energy from CpcL–PBS.

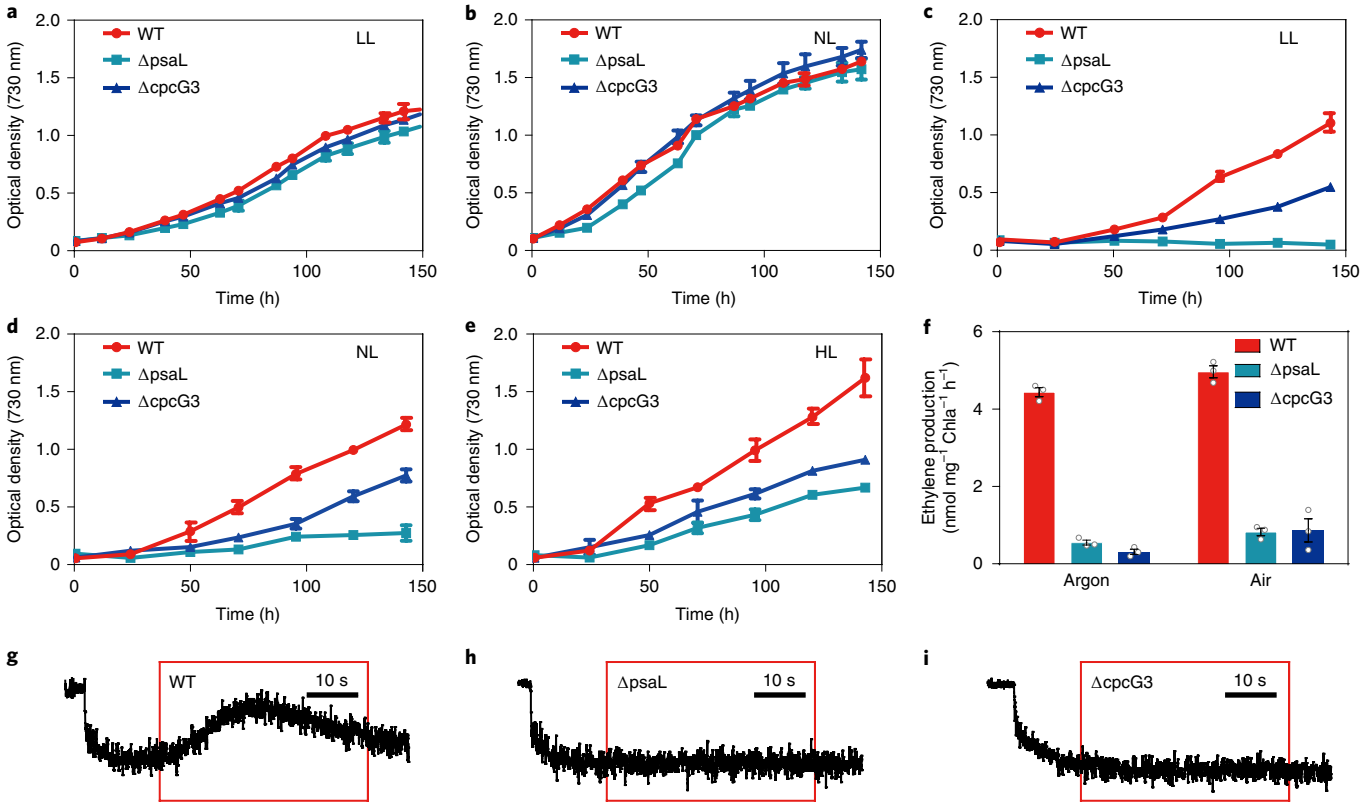

Fig. 5 | Phenotype characterization of the WT and mutant strains of *Anabaena* 7120 under different light and nitrogen conditions. a,**b**, The strains were grown in the presence of nitrate (BG11 medium) under growth light intensities of 20 μmol photons m^{-2} s^{-1} (low light, LL (**a**)) and 50 μmol photons m^{-2} s^{-1} (normal light, NL (**b**)). **c–e**, The strains were grown in the absence of combined nitrogen ($BG11_0$ medium) and the growth light intensities were 20 μmol photons m^{-2} s^{-1} (LL (**c**)), 50 μmol photons m^{-2} s^{-1} (NL (**d**)) and 200 μmol photons m^{-2} s^{-1} (high light, HL (**e**)). **f**, Measurement of nitrogenase activity as represented by ethylene production under aerobic (in air) or anaerobic (in argon) conditions. **a–f**, Error bars and centres are standard deviation and mean, respectively, and $n = 3$. **g–i**, PIRF analysis of the WT (**g**), ΔpsaL (**h**) and ΔcpcG3 (**i**). The red squares in panels **g–i** are for highlighting the curves inside the squares. Experiments in **g–i** were repeated more than three times with similar results.

Next, we examined the growth of ΔpsaL under different conditions. Similar to the *psaL* mutants in unicellular cyanobacteria[15,32], growth rate of ΔpsaL was the same as WT when grown in the presence of nitrate (Fig. 5a,b), a condition that favours linear electron transfer[36]. Their oxygen evolution rates were also similar (Supplementary Fig. 9f). In addition to linear electron transfer, PSI also drives CEF, which is important under special conditions[24,37]. We took advantage of the fact that *Anabaena* 7120 is able to form heterocysts specifically for nitrogen fixation in response to the absence of combined nitrogen and therefore can grow diazotrophically[23,24]. Heterocysts do not have PSII for oxygen evolution and the energy required for nitrogenase activity in the form of ATP is mostly generated by CEF around PSI[24]. CEF in both cyanobacteria and higher plants requires NAD(P)H dehydrogenase NDH[38] and is optimized by the formation of an NDH–PSI supercomplex[39,40]. As the NDH–PSI supercomplex formation in cyanobacteria requires CpcL–PBS[37], we studied the growth of ΔcpcG3 lacking the gene *cpcL* and also of ΔpsaL under a condition lacking combined nitrogen.

Under a low light condition, little growth was observed for ΔpsaL and the growth rate of ΔcpcG3 was much slower than WT (Fig. 5b,c), implying that the mutants could not perform nitrogen fixation properly. At higher growth light intensities, the growth rates of ΔcpcG3 were unchanged and a faster growth of ΔpsaL was observed (Fig. 5d,e); however, their growth rates were still significantly slower than WT. The filaments of the mutant strains contained patterned distribution of heterocysts (Supplementary Fig. 10a), and heterocyst frequencies of both strains were similar to WT (Supplementary Fig. 10b). Immunoblotting with anti-NifH antibodies estimated that the amount of nitrogenase in both mutants was comparable to WT 30 h after nitrogen deprivation (Supplementary Fig. 10c). However, when nitrogenase activities were measured it was found that ΔcpcG3 and ΔpsaL had much lower activities under either aerobic (in air) or anaerobic (in argon) conditions than the WT cells (Fig. 5f). This indicated that the heterocyst formation in ΔpsaL was not impaired but its nitrogen fixation activity was compromised.

The post-illumination rise of Chl fluorescence (PIRF), which measures electron donation to the interphotosystem electron pool and has been used extensively as an indicator of NDH-mediated CEF[37,41], was measured because ATP is the most important energy source for nitrogenase and its supply is almost solely dependent upon CEF in heterocysts. The PIRF was readily observed in WT when the actinic light was turned off (in red square in Fig. 5g) but it was not observed in ΔpsaL and ΔcpcG3 (Fig. 5h,i), suggesting that both CpcL–PBS and the formation of PSI tetramer are involved in CEF. When the cells in a medium depleted of carbon dioxide were illuminated with a saturating actinic light for a prolonged period of time to reduce electron acceptors in cytosol followed immediately by a weak far-red light, WT was able to oxidize P700 of PSI but ΔcpcG3 and ΔpsaL were both impaired in P700 oxidation (Supplementary Fig. 11a). When electron acceptor methyl viologen was added to the cell suspension, P700 of the mutant strains could be oxidized as efficiently as WT (Supplementary Fig. 11d), indicating

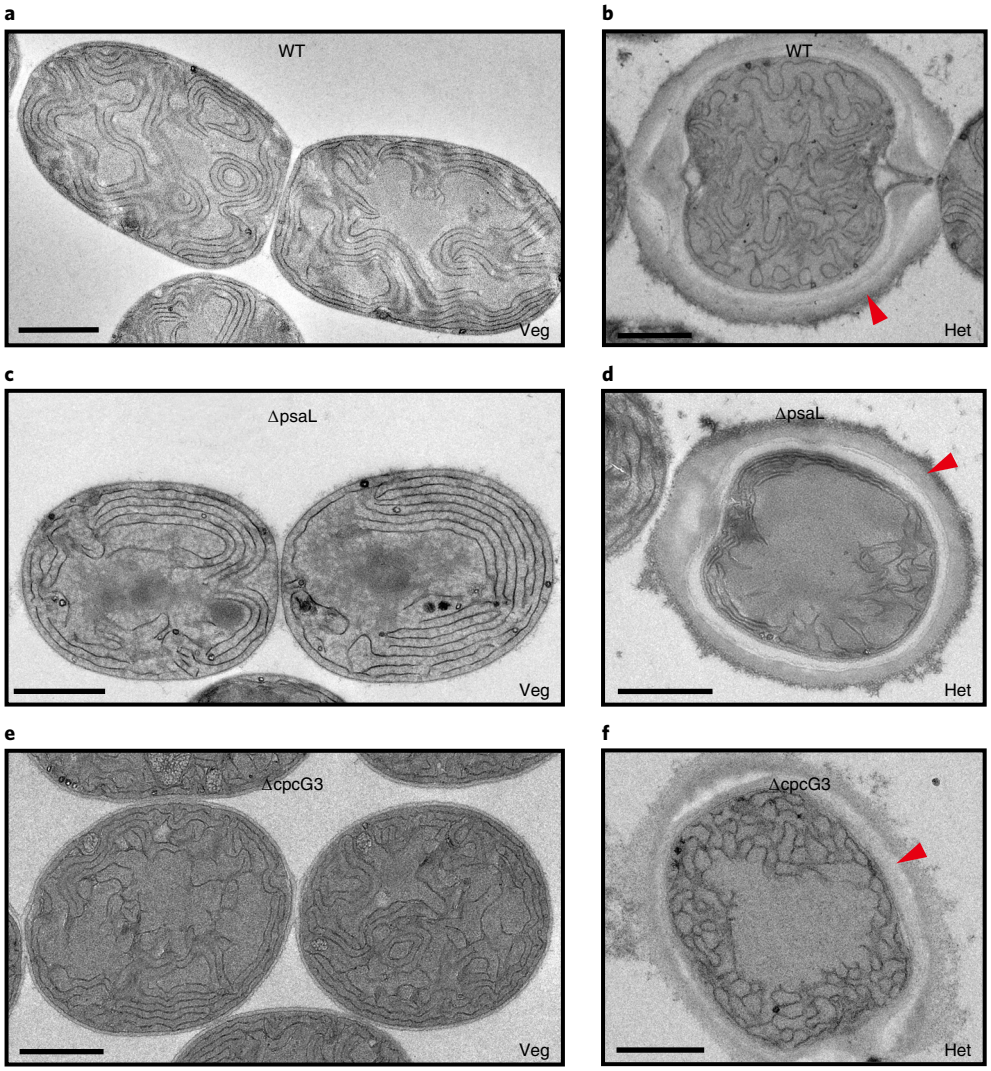

Fig. 6 | Thin-section EM images of the vegetative cells and heterocysts of *Anabaena* 7120. a–f, The cultures of WT (**a**,**b**), ΔpsaL (**c**,**d**) and ΔcpcG3 (**e**,**f**) were grown in the absence of combined nitrogen. Vegetative (Veg) cells (**a**,**c**,**e**) and heterocysts (het) (**b**,**d**,**f**) of different strains are labelled. The thick walls of heterocysts are indicated by red arrows. Scale bars, 1 μm. EM experiments were performed four times and similar observations were found on multiple positions.

that the oxidation of reduced ferredoxin by NDH complex was inhibited in both ΔpsaL and ΔcpcG3. These results, together with the growth phenotypes, indicate that CpcL–PBS and the formation of PSI tetramer are both critical to the NDH–CEF in vegetative cells as well as in heterocysts.

Accumulating evidence has shown that two physiological functions of CpcL–PBS exist: light harvesting for PSI[35,42,43] and the facilitation of the NDH–PSI supercomplex formation[37]. However, the physiological role of PSI oligomerization such as trimer and tetramer formation are not understood. It is not clear if a PSI monomer or an oligomer was involved in the NDH–CEF in the cyanobacteria. Our study provided strong evidence that the formation of tetramer of PSI in *Anabaena* 7120 is required for optimal CEF for PSI. The phenotypes of diazotrophical growth indicate that the impairment of NDH–CEF in ΔcpcG3 is less than that in ΔpsaL and therefore the formation of tetramer might be more important to NDH–CEF than CpcL–PBS.

PsaL is involved in thylakoid membrane organization

There was also a notable change in ΔpsaL in cellular organization of thylakoid membranes compared to WT cells (Fig. 6). Similar to the results from previous studies[44–46], we found that the thylakoid membranes in the WT cells were curved and located irregularly in the cytoplasm of vegetative cells (Fig. 6a), while the thylakoid membranes in WT heterocysts were more curved and irregular (Fig. 6b). In ΔpsaL vegetative cells, layers of thylakoid membranes are arranged in parallel in the peripheral of the cells (Fig. 6c), an arrangement of thylakoids often found in nonheterocystous cyanobacteria such as *Phomidium* sp.[47]. The thylakoid membranes in heterocysts of ΔpsaL also showed an arrangement of several layers of parallel membranes that were mostly located at the peripheral areas of heterocysts (Fig. 6d). The organization of the thylakoid membranes in ΔcpcG3 was nearly unaltered compared to WT (Fig. 6e,f), suggesting that the tetramer formation is important to the thylakoid membrane organization. A significant change of thylakoid membrane in the *psaL* mutant of *Synechocystis* 6803 occurred at an elevated growth temperature[48], indicating that the membrane organization could be influenced by trimer formation of PSI at a stressed condition.

At present, little is known about the mechanism of thylakoid organization in cyanobacteria. Nevertheless, our study provided

evidence that the oligomerization state of PSI and possibly the interaction of PSI with the NDH complex played a crucial role in the organization of thylakoid membranes in *Anabaena* 7120. Evolutionarily, heterocyst differentiation was a response of cyanobacteria to an increasing oxygen concentration on Earth[24]. The fact that heterocyst-forming cyanobacteria have tetrameric PSI implies that it could be more effective in its functions in heterocysts, such as interacting with the NDH complex and generating a proton gradient by CEF for ATP biosynthesis in heterocysts. Although NDH–PSI supercomplexes have not been isolated in heterocystous cyanobacteria, the results presented in this work clearly show that there is an NDH–PSI supercomplex in *Anabaena* 7120 as well as in *Synechocystis* 6803[37]. The NDH-1L–PSI supercomplex should be an extremely large complex and it is a challenging task to isolate it for structural study. The cryo-EM structure of PSI present here and the recent success in determining the L-shaped structure of the NDH-1L complex by cryo-EM[49] will undoubtedly shed light on our understanding of the interaction between NDH and PSI complexes.

Conclusion

In summary, we provided structural analysis of a unique tetrameric PSI complex found in heterocyst-forming cyanobacterial species and showed that oligomerization of PSI is required for optimal CEF. Our data also revealed a functional link between the formation of PSI oligomers and the thylakoid membrane organization, highlighting the presence of a higher order spatial arrangement of photosystem complexes, CpcL–PBS and NDH complexes in thylakoid membranes.

Methods

Culture conditions. The WT and the mutant strains of *Anabaena* 7120 were grown in BG11 or $BG11_0$ media[50] at 25 °C. The light intensity was approximately 50 and 20 μmol photons $m^{-2} s^{-1}$ for normal light and low light growth, respectively. When needed, the antibiotic neomycin and/or erythromycin were added to cultures at concentrations of 25 μg ml^{-1} and 10 μg ml^{-1}, respectively. Cell density was determined by measuring optical density at 730 nm.

Construction of mutants. The mutant ΔcpcG3 lacking *cpcL* was constructed as described[34]. The mutant ΔpsaL was constructed as follows: the upstream and downstream region of *all0107* and a DNA fragment encoding a kanamycin resistance cassette (*Kan*^{r}) were amplified by polymerase chain reaction (PCR) with primer pairs of P1/P2, P3/P4 and P5/P6 (Supplementary Table 1), respectively. A pRL277 plasmid for transformation of *Anabaena* 7120 by conjugation was digested with XhoI/SacI and the resulting fragment, together with all three PCR products, were combined in a Gibson Assembly Reaction[51] to generate the corresponding plasmid. This plasmid was used to transform the WT strain to generate the mutant ΔpsaL according to a standard procedure[52]. The mutant was verified by PCR.

Isolation of thylakoid membranes. Cells were harvested by centrifugation and resuspended in buffer A (50 mM MES–sodium hydroxide (NaOH) pH 6.5, 0.4 M sucrose, 50 mM sodium chloride (NaCl)). The cell breakage was performed at 4 °C using an ultra-high-pressure cell disrupter (JNBIO, JN-Mini) at 1,000 bar. After removal of unbroken cells by centrifugation at a speed of 3,000*g* for 15 min, the resulting supernatant was diluted with equal volume buffer B (50 mM MES–NaOH pH 6.5, 50 mM NaCl) and centrifuged at 20,000*g* for 30 min at 4 °C to separate thylakoid membranes and soluble proteins. The resulting pellets (crude thylakoid membranes) were washed twice with buffer C (50 mM MES–NaOH pH 6.5, 500 mM NaCl) to remove nonspecifically attached proteins. The thylakoid membranes were resuspended in a low salt buffer D (50 mM MES–NaOH pH 6.5, 10 mM magnesium chloride ($MgCl_2$), 5 mM calcium chloride ($CaCl_2$), 25% (w/v) glycerol)[35] and stored at −80 °C.

PSI complex purification. Thylakoid membranes (1 mg Chl ml^{-1}) were solubilized with 2% β-*n*-Dodecyl β-D-maltoside (Amresco) on ice and gentle stirred for 30 min, followed by centrifugation at 20,000*g* for 30 min at 4 °C. The supernatant was diluted with two volumes of buffer E (50 mM MES–NaOH pH 6.5, 10 mM $MgCl_2$, 5 mM $CaCl_2$) and fractionated by sucrose-density gradient ultracentrifugation at 130,000*g*, 4 °C for 18 h (Beckman SW40 rotor). The green bands (Supplementary Fig. 1) after centrifugation were collected and examined with an electron microscope (Tecnai G^2 Spirit, FEI) after negative staining[34].

Nitrogenase activity measurement. Nitrogenase activity was measured as acetylene reduction as described[53] with minor modifications. Samples (3 ml) from the cultures were transferred to 22.5 ml glass vials. The vials were either bubbled with air or purged with argon before acetylene was added to 10% (v/v). After 2 h incubation under illumination of 20 μmol photon $m^{-2} s^{-1}$, 1 ml of gas in the vials was extracted to measure ethylene concentrations by gas chromatography using a Shimadzu GC-2014. Specific nitrogenase activities were calculated on the basis of Chl-a content of the cells.

Thin-section EM. Thin-section EM was performed according to the procedures described previously[54]. The samples were fixed by overnight incubation with 4% paraformaldehyde/2.5% glutaraldehyde in 0.1 M phosphate buffer (pH 7.4) at 4 °C. The samples were washed several times with phosphate buffer and were post-fixed in 2% potassium permanganate in phosphate buffer for 4 h at room temperature in the dark. After rinsing several times with distilled water, the samples were embedded in agarose (Sigma-Aldrich, A9414) and cut into 1 × 1 × 1 mm^3 blocks. The small blocks were stained with 2% aqueous uranyl acetate overnight at 4 °C. Following several washes with distilled water, blocks were dehydrated through a graded alcohol series (30, 50 and 70% and 85, 95 and 100%) and subsequently embedded in Spurr's resin (SPI Supplies). Ultra-thin sections (70 nm) were obtained using an ultramicrotome (UC7, Leica) and mounted on copper grids with a single slot. Sections were examined and imaged with an electron microscope (Tecnai G^2 Spirit, FEI) at 120 kV.

Fluorescence emission measurement. Fluorescence emission spectra at 77 K were obtained as described previously[55]. Cells were first adjusted to an optical density at wavelength 730 nm (OD_{730nm}) of 0.8 and were incubated in the dark for 5 min to generate state 2 conditions or illuminated with blue light (by 460 nm short-pass filter) at 100 μmol photons $m^{-2} s^{-1}$ for 3 min in the presence of DCMU (3-(3,4-dichlorophenyl)-1,1-dimethylurea) to produce state 1 conditions before freezing in liquid nitrogen. Fluorescence emission spectra were collected using a Nanolog FL3-2iHR fluorometer with the excitation wavelengths at 440 nm for excitation of Chl or at 590 nm for excitation of PBS.

Oxygen evolution measurement. The oxygen evolution rate from cells of *Anabaena* 7120 was measured using an oxygen electrode system (Hansatech Instruments) at 28 °C using a circulating water bath. Light was provided by a 300 W tungsten light source and passed through a 16% attenuate neutrol filter. Cells were harvested and adjusted to OD_{730nm} of 1.0. Cells were dark-adapted in the presence of 10 mM hydrogen carbonate as an electron acceptor for 2 min and illuminated with a light intensity of 360 μmol photons $m^{-2} s^{-1}$.

P700 measurement. P700 of PSI was measured using a dual-pulse-amplitude-modulation (PAM)-100 instrument (Heinz Walz) as described[43]. Cell culture was adjusted to OD_{730nm} of 3.0 and kept in the dark for 5 min before continuous monitoring of $P700^+$ signals started. For measurement of the effect of far-red light (FR; >720 nm, 0.3 μmol $m^{-2} s^{-1}$), the FR was first turned on for 20 s before an actinic light (2,800 μmol $m^{-2} s^{-1}$) was turned on for 30 s. When the actinic light was turned off, the $P700^+$ signal was monitored under FR. Methyl viologen was added to the culture when required at concentrations indicated in the text.

Post-illumination of fluorescence rise. Post-illumination of fluorescence was measured by the pulse-amplitude fluorimeter model dual-PAM-100 (Heinz Walz) as described[56,57]. Cells were harvested and adjusted to OD_{730nm} of 1.0. The samples were inserted into the PAM fluorometer and incubated in the dark for 5 min before actinic light (200 μmol $m^{-2} s^{-1}$) was turned on for 30 s, during which short saturating pulses were applied every 5 s six times. The transient increase in chlorophyll fluorescence after turning off the actinic light was measured.

Confocal microscopy. Confocal images of the cells were obtained with a confocal microscope (Leica TCS SP8, Leica) equipped with a HCX PL APO ×63 oil objective. The samples were excited with 561 nm (White Light Laser) laser. The detection wavelength range was set to 530–700 nm. All images were acquired with the LAS AF software (Leica). Deconvolution processing was performed with Huygens Professional software (Scientific Volume Imaging).

Cryo-EM data collection and image processing. Tetrameric PSI complexes were purified from cyanobacterium *Anabaena* 7120 using sucrose-density gradient centrifugation. Initial attempts of cryo-grid preparation showed that PSI tetramers tended to dissociate and GraFix[25] was therefore used in the last centrifugation step to generate cross-linked samples for cryo-EM analysis in the presence of 0–0.05% glutaraldehyde in gradients, from top to bottom. Fractions (2 ml) of tetramers were further concentrated to 0.5 ml using a centrifugal filter (3,000*g* at 4 °C) three times, with buffer exchanged to 50 mM MES–NaOH (pH 6.5), 10 mM $MgCl_2$, 5 mM $CaCl_2$, 0.03% *n*-Dodecyl β-D-maltoside. A final chlorophyll concentration of 3 mg ml^{-1} of PSI complexes was used for cryo-grid preparation. Aliquots (4 μl) of the sample were placed onto glow-discharged holey gold grids (Quantifoil R1.2/1.3) and the grids were prepared using an FEI Vitrobot Mark IV (4 °C and 100% humidity). Cryo-grids were first screened in a Talos Arctica of 200 kV equipped with a CETA camera. Data collection was performed with an FEI Titan Krios G2 microscope of 300 kV with Gatan K2 (GIF) direct electron detector using the

semi-automatic program of SerialEM[58]. The nominal magnification of ×130,000 and the defocus range between −1.8 and −2.3 µm were used for data collection. For each image stack (40 frames), a total dose is about 58 electrons Å^{-2} at a calibrated pixel size 1.052 Å.

A total of 2,301 raw movies were obtained and beam-induced motion was corrected using MotionCor2 (ref. [59]). The program Gctf[60] was used to estimate the contrast transfer function (CTF) parameters of drift-corrected micrographs. An initial set of 10,000 particles was manually picked and used as two-dimensional (2D) templates for automatic particle-picking in RELION2.0 (ref. [61]). As a result, ~291,000 particles were auto-picked and subjected to one round (25 iterations) of 2D classification (Supplementary Fig. 2). Particles from good 2D classes (around 176,000) were subjected to two rounds of three-dimensional (3D) classification. The initial 3D reference was generated using RELION2.0. A final set of particles (71,600) were kept for high-resolution refinement. To improve the performance of 3D refinement, we recentred and re-extracted the particles from the dose-weighted images and the local defocus values were generated using Gctf. A soft-edged mask was also applied in 3D refinement, leading to a 2.82-Å density map of the tetrameric PSI complex (gold-standard FSC 0.143 criteria). CTF refinement and Bayesian polishing were subsequently applied using RELION3.0[62]. This improved the resolution to 2.49 Å and 2.37 Å, respectively (Supplementary Fig. 2). The post-processing of the map was carried out using RELION3.0 with an automatically estimated B-factor. The local resolution map was generated by ResMap[63].

Model building and refinement. Crystal structure of the trimeric PSI (Protein Data Bank code 1JB0)[7] was used as the initial template for modelling. The atomic model was first docked into the density map using the University of California San Francisco Chimera[64]. Due to the high sequence conservation, the amino acid sequences of 12 subunits of a monomer were manually replaced with their own sequences of *Anabaena* 7120 using Coot[65]. A few loops and insertions were built de novo from sequences. The high-resolution features of the map allowed the accurate placement of carbonyl oxygens of peptide chains in many regions of the density map. The phytyls of some chlorophylls and a dozen lipid molecules were also well-defined. The model building of the second monomer was performed manually using the first one as the initial model. A tetramer PSI model was obtained by rotating the dimer 180°. Real-space refinement was performed using Phenix[66], with geometry and secondary structure restraints applied. The final atomic model was evaluated using Molprobity[67] and the statistics of data collection and model validation are summarized in Supplementary Table 2. Figure preparation was present with the University of California San Francisco Chimera and Pymol (http://pymol.org).

Molecular dynamics simulation. A number of membrane protein systems have been validated by enhanced sampling MD simulations[68–71]. We mixed 3,264 lipid molecules proportionally and randomly to bilayer forming using CHARMM–GUI[72], then solvated in a 32.8×32.8×12 nm^3 box and neutralized with sodium ions. The constructed thylakoid membrane system was equilibrated for 10 ns with CHARMM36 force field[73] using the NAMD simulation package[74]. The four PSI monomers were separated along the membrane plane from cryo-EM structure to an interfacial distance of more than 2 nm between two adjacent monomers (Supplementary Fig. 5a). A collective variable, distance root mean square deviation (DRMSD), was defined to represent the relative distance between two monomers. DRMSD calculates the root mean square deviation of the distances between atoms in one monomer and atoms in another monomer to those distances in a reference structure. If the cryo-EM structure is set to reference structure, the value of DRMSD is zero and the value for the separated structure is approximately 2 nm. The separated structure was embedded in the equilibrated thylakoid membrane with overlapped lipids removed. The PSI-membrane system was coarse-grained to Martini model[75], where the topology and force field of proteins were derived by Martinize script[76] and those of lipids and cofactors referred from previous studies on thylakoids[77] or photosystems[78]. The coarse-grained system was solvated by Martini water and neutralized by Martini sodium ions. All coarse-grained simulations were performed using the GROMACS package[79]. The whole system was subjected to energy minimization using the steepest descent algorithm and gradually heated to 330 K under NVT (canonical) ensemble and equilibrated under NPT (isothermal-isobaric) ensemble. The leap-frog verlet integrator with a time step of 10 fs was used for coarse-grained simulation. Reaction-field method[80] with a relative dielectric constant of 15 was used to treat electrostatic interactions with a cut-off distance of 1.2 nm. The same cut-off value was chosen for treating van der Waals interactions. The temperature was kept at 330 K using the V-rescale thermostat[81] with a coupling constant of 1 ps. The pressure was semi-isotropically coupled to 1 bar using Parrinello–Rahman barostat[82] with a coupling constant of 4 ps and compressibility of 3×10^{-4} bar^{-1}.

The production run was performed with Metadynamics[83] on the collective variable DRMSD by PLUMED plug-in[84] for 1 µs and repeated eight times independently. Metadynamics is an enhanced sampling method that can add history-dependent bias potential to fill the minima in the free-energy surface as a function of the collective variables. Consequently, it allows the system to escape from a local free-energy minima and cross the energy barrier to another minima. Within a 1-µs simulation, four monomers assembled to a tetramer (Supplementary Fig. 5b) that had no tendency to disassemble (Supplementary Fig. 5c). It was demonstrated that the assembled structure had lower energy than a separated structure and was more stable. In addition, interface I assembles faster than interface II. We analysed the distribution of four classes of lipids changing over time in the assembly process, and determined that MGDG is significantly higher than other lipids in the central hole of the PSI tetramer (Supplementary Fig. 5d). In addition, peripheral lipids diffuse to the heterogeneous phase after the assembly process. SQDG and MGDG are enriched around the assembled PSI (Supplementary Fig. 5e). We calculated the electrostatic and van der Waals interactions between adjacent PSI monomers and between PSI and lipids, and deduced that the van der Waals interactions between PSI and SQDG, MGDG are the key driving force for the tetramer assembly (Fig. 4).

Reporting Summary. Further information on research design is available in the Nature Research Reporting Summary linked to this article.

Data availability

Atomic coordinates have been deposited in the Protein Data Bank under the accession code 6K61. The cryo-EM density map has been uploaded to the Electron Microscopy Data Bank under the accession code EMD-9918. All other data can be obtained from the corresponding authors upon reasonable request.

Received: 31 March 2019; Accepted: 5 September 2019;
Published online: 8 October 2019

References

1. Nelson, N. & Yocum, C. F. Structure and function of photosystems I and II. *Annu. Rev. Plant Biol.* **57**, 521–565 (2006).
2. Wei, X. et al. Structure of spinach photosystem II–LHCII supercomplex at 3.2 Å resolution. *Nature* **534**, 69–74 (2016).
3. van Bezouwen, L. S. et al. Subunit and chlorophyll organization of the plant photosystem II supercomplex. *Nat. Plants* **3**, 17080 (2017).
4. Umena, Y., Kawakami, K., Shen, J. R. & Kamiya, N. Crystal structure of oxygen-evolving photosystem II at a resolution of 1.9 Å. *Nature* **473**, 55–60 (2011).
5. Suga, M. et al. Native structure of photosystem II at 1.95 Å resolution viewed by femtosecond X-ray pulses. *Nature* **517**, 99–103 (2015).
6. Takahashi, Y., Koike, H. & Katoh, S. Multiple forms of chlorophyll–protein complexes from a thermophilic cyanobacterium *Synechococcus* sp. *Arch. Biochem Biophys.* **219**, 209–218 (1982).
7. Jordan, P. et al. Three-dimensional structure of cyanobacterial photosystem I at 2.5 Å resolution. *Nature* **411**, 909–917 (2001).
8. Su, X. et al. Structure and assembly mechanism of plant C2S2M2-type PSII–LHCII supercomplex. *Science* **357**, 815–820 (2017).
9. Mazor, Y., Borovikova, A., Caspy, I. & Nelson, N. Structure of the plant photosystem I supercomplex at 2.6 Å resolution. *Nat. Plants* **3**, 17014 (2017).
10. Qin, X., Suga, M., Kuang, T. & Shen, J. R. Photosynthesis. Structural basis for energy transfer pathways in the plant PSI–LHCI supercomplex. *Science* **348**, 989–995 (2015).
11. Mazor, Y., Nataf, D., Toporik, H. & Nelson, N. Crystal structures of virus-like photosystem I complexes from the mesophilic cyanobacterium *Synechocystis* PCC 6803. *eLife* **3**, e01496 (2013).
12. Pan, X. et al. Structure of the maize photosystem I supercomplex with light-harvesting complexes I and II. *Science* **360**, 1109–1113 (2018).
13. Malavath, T., Caspy, I., Netzer-El, S. Y., Klaiman, D. & Nelson, N. Structure and function of wild-type and subunit-depleted photosystem I in *Synechocystis*. *Biochim. Biophys. Acta Bioenerg.* **1859**, 645–654 (2018).
14. Rögner, M., Mühlenhoff, U., Boekema, E. J. & Witt, H. T. Mono-, di- and trimeric PS I reaction center complexes isolated from the thermophilic cyanobacterium *Synechococcus* sp. *Biochim. Biophys. Acta Bioenerg.* **1015**, 415–424 (1990).
15. Chitnis, V. P. & Chitnis, P. R. PsaL subunit is required for the formation of photosystem-I trimers in the cyanobacterium *Synechocystis* sp. PCC 6803. *Febs Lett.* **336**, 330–334 (1993).
16. Xu, Q. et al. Mutational analysis of photosystem I polypeptides in the cyanobacterium *Synechocystis* sp. PCC 6803. targeted inactivation of psaI reveals the function of psaI in the structural organization of psaL. *J. Biol. Chem.* **270**, 16243–16250 (1995).
17. Ben-Shem, A., Frolow, F. & Nelson, N. Light-harvesting features revealed by the structure of plant photosystem I. *Photosynth Res* **81**, 239–250 (2004).
18. Nelson, N. & Ben-Shem, A. The structure of photosystem I and evolution of photosynthesis. *Bioessays* **27**, 914–922 (2005).
19. Amunts, A. & Nelson, N. Functional organization of a plant photosystem I: evolution of a highly efficient photochemical machine. *Plant Physiol. Biochem.* **46**, 228–237 (2008).
20. Semchonok, D. A., Li, M., Bruce, B. D., Oostergetel, G. T. & Boekema, E. J. Cryo-EM structure of a tetrameric cyanobacterial photosystem I complex reveals novel subunit interactions. *Biochim. Biophys. Acta* **1857**, 1619–1626 (2016).

21. Li, M., Semchonok, D. A., Boekema, E. J. & Bruce, B. D. Characterization and evolution of tetrameric photosystem I from the thermophilic cyanobacterium *Chroococcidiopsis* sp. TS-821. *Plant Cell* **26**, 1230–1245 (2014).
22. Watanabe, M., Kubota, H., Wada, H., Narikawa, R. & Ikeuchi, M. Novel supercomplex organization of photosystem I in anabaena and cyanophora paradoxa. *Plant Cell Physiol.* **52**, 162–168 (2011).
23. Flores, E., Picossi, S., Valladares, A. & Herrero, A. Transcriptional regulation of development in heterocyst-forming cyanobacteria. *Biochim. Biophys. Acta Gene Regul. Mech.* **1862**, 673–684 (2019).
24. Wolk, C. P., Ernst, A. & Elhai, J. in *The Molecular Biology of Cyanobacteria* (ed. Bryant, D. A.) 769–823 (Springer Netherlands, 1994).
25. Kastner, B. et al. GraFix: sample preparation for single-particle electron cryomicroscopy. *Nat. Methods* **5**, 53–55 (2008).
26. Fromme, P., Jordan, P. & Krauss, N. Structure of photosystem I. *Biochim. Biophys. Acta* **1507**, 5–31 (2001).
27. Grotjohann, I. & Fromme, P. Structure of cyanobacterial photosystem I. *Photosynth. Res.* **85**, 51–72 (2005).
28. Mizusawa, N., Sakata, S., Sakurai, I., Sato, N. & Wada, H. Involvement of digalactosyldiacylglycerol in cellular thermotolerance in *Synechocystis* sp. PCC 6803. *Arch. Microbiol.* **191**, 595–601 (2009).
29. Mizusawa, N., Sakurai, I., Sato, N. & Wada, H. Lack of digalactosyldiacylglycerol increases the sensitivity of *Synechocystis* sp. PCC 6803 to high light stress. *FEBS Lett.* **583**, 718–722 (2009).
30. Sato, N. Roles of the acidic lipids sulfoquinovosyl diacylglycerol and phosphatidylglycerol in photosynthesis: their specificity and evolution. *J. Plant Res.* **117**, 495–505 (2004).
31. Domonkos, I. et al. Phosphatidylglycerol is essential for oligomerization of photosystem I reaction center. *Plant Physiol.* **134**, 1471–1478 (2004).
32. Schluchter, W. M., Shen, G., Zhao, J. & Bryant, D. A. Characterization of psaI and psaL mutants of *Synechococcus* sp. strain PCC 7002: a new model for state transitions in cyanobacteria. *Photochem. Photobio.* **64**, 53–66 (1996).
33. Aspinwall, C. L., Sarcina, M. & Mullineaux, C. W. Phycobilisome mobility in the cyanobacterium *Synechococcus* sp. PCC7942 is influenced by the trimerisation of photosystem I. *Photosynth Res* **79**, 179 (2004).
34. Chang, L. et al. Structural organization of an intact phycobilisome and its association with photosystem II. *Cell Res.* **25**, 726–737 (2015).
35. Watanabe, M. et al. Attachment of phycobilisomes in an antenna-photosystem I supercomplex of cyanobacteria. *Proc. Natl Acad. Sci. USA* **111**, 2512–2517 (2014).
36. Myers, J. Is there significant cyclic electron flow around photoreaction 1 in cyanobacteria? *Photosynth. Res.* **14**, 55–69 (1987).
37. Gao, F. et al. The NDH-1L–PSI supercomplex is important for efficient cyclic electron transport in cyanobacteria. *Plant Physiol.* **172**, 1451–1464 (2016).
38. Peltier, G., Aro, E. M. & Shikanai, T. NDH-1 and NDH-2 plastoquinone reductases in oxygenic photosynthesis. *Annu. Rev. Plant Biol.* **67**, 55–80 (2016).
39. Peng, L. & Shikanai, T. Supercomplex formation with photosystem I is required for the stabilization of the chloroplast NADH dehydrogenase-like complex in *Arabidopsis*. *Plant Physiol.* **155**, 1629–1639 (2011).
40. Kato, Y., Sugimoto, K. & Shikanai, T. NDH-PSI supercomplex assembly precedes full assembly of the NDH complex in chloroplast. *Plant Physiol.* **176**, 1728–1738 (2018).
41. Xu, M., Lv, J., Fu, P. & Mi, H. Oscillation kinetics of post-illumination increase in Chl fluorescence in cyanobacterium *Synechocystis* PCC 6803. *Front. Plant Sci.* **7**, 108 (2016).
42. Kondo, K., Mullineaux, C. W. & Ikeuchi, M. Distinct roles of CpcG1-phycobilisome and CpcG2-phycobilisome in state transitions in a cyanobacterium *Synechocystis* sp. PCC 6803. *Photosynth. Res.* **99**, 217–225 (2009).
43. Deng, G., Liu, F., Liu, X. & Zhao, J. Significant energy transfer from CpcG2-phycobilisomes to photosystem I in the cyanobacterium *Synechococcus* sp. PCC 7002 in the absence of ApcD-dependent state transitions. *FEBS Lett.* **586**, 2342–2345 (2012).
44. Bauer, C. C., Buikema, W. J., Black, K. & Haselkorn, R. A short-filament mutant of *Anabaena* sp. strain PCC-7120 that fragments in nitrogen-deficient medium. *J. Bacteriol.* **177**, 1520–1526 (1995).
45. Shi, L. et al. Two genes encoding protein kinases of the HstK family are involved in synthesis of the minor heterocyst-specific glycolipid in the cyanobacterium *Anabaena* sp. strain PCC 7120. *J. Bacteriol.* **189**, 5075–5081 (2007).
46. Zheng, Z. G. et al. An amidase is required for proper intercellular communication in the filamentous cyanobacterium *Anabaena* sp. PCC 7120. *Proc. Natl Acad. Sci. USA* **114**, E1405–E1412 (2017).
47. Ohki, K. & Fujita, Y. Photoregulation of phycobilisome structure during complementary chromatic adaptation in the marine cyanophyte *Phormidium* sp. C86. *J. Phycol.* **28**, 803–808 (1992).
48. Klodawska, K. et al. Elevated growth temperature can enhance photosystem I trimer formation and affects xanthophyll biosynthesis in cyanobacterium *Synechocystis* sp. PCC 6803 cells. *Plant Cell Physiol.* **56**, 558–571 (2015).
49. Schuller, J. M. et al. Structural adaptations of photosynthetic complex I enable ferredoxin-dependent electron transfer. *Science* **363**, 257–260 (2019).
50. Rippka, R., Deruelles, J., Waterbury, J. B., Herdman, M. & Stanier, R. Y. Generic assignments, strain histories and properties of pure cultures of cyanobacteria. *J. Gen. Microbiol.* **111**, 1–61 (1979).
51. Gibson, D. G. et al. Enzymatic assembly of DNA molecules up to several hundred kilobases. *Nat. Methods* **6**, 343–345 (2009).
52. Elhai, J. & Wolk, C. P. Conjugal transfer of DNA to cyanobacteria. *Methods Enzymol.* **167**, 747–754 (1988).
53. Zhao, W., Ye, Z. & Zhao, J. RbrA, a cyanobacterial rubrerythrin, functions as a FNR-dependent peroxidase in heterocysts in protection of nitrogenase from damage by hydrogen peroxide in *Anabaena* sp. PCC 7120. *Mol. Microbiol.* **66**, 1219–1230 (2007).
54. Black, K., Buikema, W. J. & Haselkorn, R. The hglK gene is required for localization of heterocyst-specific glycolipids in the cyanobacterium *Anabaena* sp. strain PCC 7120. *J. Bacteriol.* **177**, 6440–6448 (1995).
55. Zhao, J., Shen, G. & Bryant, D. A. Photosystem stoichiometry and state transitions in a mutant of the cyanobacterium *Synechococcus* sp. PCC 7002 lacking phycocyanin. *Biochim. Biophys. Acta* **1505**, 248–257 (2001).
56. Liu, X. et al. Effects of PSII manganese-stabilizing protein succinylation on photosynthesis in the model cyanobacterium *Synechococcus* sp. PCC 7002. *Plant Cell Physiol.* **59**, 1466–1482 (2018).
57. Shikanai, T. et al. Directed disruption of the tobacco ndhB gene impairs cyclic electron flow around photosystem I. *Proc. Natl Acad. Sci. USA* **95**, 9705–9709 (1998).
58. Mastronarde, D. N. Automated electron microscope tomography using robust prediction of specimen movements. *J. Struct. Biol.* **152**, 36–51 (2005).
59. Zheng, S. Q. et al. MotionCor2: anisotropic correction of beam-induced motion for improved cryo-electron microscopy. *Nat. Methods* **14**, 331–332 (2017).
60. Zhang, K. Gctf: real-time CTF determination and correction. *J. Struct. Biol.* **193**, 1–12 (2016).
61. Kimanius, D., Forsberg, B. O., Scheres, S. H. & Lindahl, E. Accelerated cryo-EM structure determination with parallelisation using GPUs in RELION-2. *eLife* **5**, e18722 (2016).
62. Zivanov, J. et al. New tools for automated high-resolution cryo-EM structure determination in RELION-3. *eLife* **7**, e42166 (2018).
63. Kucukelbir, A., Sigworth, F. J. & Tagare, H. D. Quantifying the local resolution of cryo-EM density maps. *Nat. Methods* **11**, 63–65 (2014).
64. Pettersen, E. F. et al. UCSF Chimera: a visualization system for exploratory research and analysis. *J. Comput. Chem.* **25**, 1605–1612 (2004).
65. Emsley, P., Lohkamp, B., Scott, W. G. & Cowtan, K. Features and development of coot. *Acta Crystallogr. D* **66**, 486–501 (2010).
66. Adams, P. D. et al. PHENIX: a comprehensive python-based system for macromolecular structure solution. *Acta Crystallogr. D* **66**, 213–221 (2010).
67. Chen, V. B. et al. MolProbity: all-atom structure validation for macromolecular crystallography. *Acta Crystallogr. D* **66**, 12–21 (2010).
68. Cao, L.-R. et al. Recent developments in using molecular dynamics simulation techniques to study biomolecules. *Acta Physico-Chimica Sinica* **33**, 1354–1365 (2017).
69. Peng, X., Zhang, Y., Chu, H. & Li, G. Free energy simulations with the AMOEBA polarizable force field and metadynamics on GPU platform. *J. Comput. Chem.* **37**, 614–622 (2016).
70. Peng, X. et al. Accurate evaluation of ion conductivity of the gramicidin a channel using a polarizable force field without any corrections. *J. Chem. Theory Comput.* **12**, 2973–2982 (2016).
71. Peng, X. et al. Integrating multiple accelerated molecular dynamics to improve accuracy of free energy calculations. *J. Chem. Theory Comput.* **14**, 1216–1227 (2018).
72. Lee, J. et al. CHARMM-GUI input generator for NAMD, GROMACS, AMBER, OpenMM, and CHARMM/OpenMM simulations using the CHARMM36 additive force field. *J. Chem. Theory Comput.* **12**, 405–413 (2016).
73. Klauda, J. B. et al. Update of the CHARMM all-atom additive force field for lipids: validation on six lipid types. *J. Phys. Chem. B* **114**, 7830–7843 (2010).
74. Phillips, J. C. et al. Scalable molecular dynamics with NAMD. *J. Comput. Chem.* **26**, 1781–1802 (2005).
75. Monticelli, L. et al. The MARTINI coarse-grained force field: extension to proteins. *J. Chem. Theory Comput.* **4**, 819–834 (2008).
76. de Jong, D. H. et al. Improved parameters for the martini coarse-grained protein force field. *J. Chem. Theory Comput.* **9**, 687–697 (2013).
77. van Eerden, F. J., de Jong, D. H., de Vries, A. H., Wassenaar, T. A. & Marrink, S. J. Characterization of thylakoid lipid membranes from cyanobacteria and higher plants by molecular dynamics simulations. *Biochim. Biophys. Acta* **1848**, 1319–1330 (2015).
78. de Jong, D. H. et al. Atomistic and coarse grain topologies for the cofactors associated with the photosystem II core complex. *J. Phys. Chem. B* **119**, 7791–7803 (2015).
79. van der Spoel, D. et al. GROMACS: fast, flexible, and free. *J. Comput. Chem.* **26**, 1701–1718 (2005).

80. Tironi, I. G., Sperb, R., Smith, P. E. & Vangunsteren, W. F. A generalized reaction field method for molecular-dynamics simulations. *J. Chem. Phys.* **102**, 5451–5459 (1995).
81. Bussi, G., Donadio, D. & Parrinello, M. Canonical sampling through velocity rescaling. *J. Chem. Phys.* **126**, 014101 (2007).
82. Parrinello, M. & Rahman, A. Polymorphic transitions in single-crystals: a new molecular-dynamics method. *J. Appl. Phys.* **52**, 7182–7190 (1981).
83. Laio, A. & Parrinello, M. Escaping free-energy minima. *Proc. Natl Acad. Sci. USA* **99**, 12562–12566 (2002).
84. Tribello, G. A., Bonomi, M., Branduardi, D., Camilloni, C. & Bussi, G. PLUMED 2: new feathers for an old bird. *Comput. Phys. Commun.* **185**, 604–613 (2014).

Acknowledgements

We thank the Electron Microscopy Laboratory of Peking University and the cryo-EM platform of Peking University for cryo-EM data collection. We also thank the Core Facilities at School of Life Sciences Peking University for assistance with thin-section EM sample preparation and image analysis. The computation was supported by High-Performance Computing Platform of Peking University. The work was funded by the Ministry of Science and Technology of China (grant nos. 2016YFA0500700 to N.G. and 2015CB150101 and 2017YFA503703 to J.Z.), the National Natural Science Foundation of China (grant nos. 31725007 and 31630087 to N.G., 91851118 to J.Z., and 21625302 and 21573217 to G.L.).

Author contributions

N.G. and J.Z. conceived the project. Y.L. purified photosystem I samples. L.Z. and Y.L. collected cryo-EM data. L.Z., C.M. and N.L. processed the cryo-EM data. L.Z., Y.L., X.L. and K.Z. conducted biochemical analysis. G.L. designed the MD strategy. G.L., Q.Z., Y.Z. and H.C. performed simulations. G.L. and Q.Z. analysed the simulation data. L.Z., Y.L., G.L., N.G. and J.Z. wrote the manuscript. All authors discussed and commented on the results and the manuscript.

Competing interests

The authors declare no competing interests.

Additional information

Supplementary information is available for this paper at https://doi.org/10.1038/s41477-019-0525-6.

Correspondence and requests for materials should be addressed to G.L., J.Z. or N.G.

Peer review information *Nature Plants* thanks Mei Li, Christopher Gisriel and the other, anonymous, reviewer for their contribution to the peer review of this work.

Reprints and permissions information is available at www.nature.com/reprints.

Publisher's note Springer Nature remains neutral with regard to jurisdictional claims in published maps and institutional affiliations.

© The Author(s), under exclusive licence to Springer Nature Limited 2019

nature research

Corresponding author(s): Guohui Li, Jindong Zhao and Ning Gao

Last updated by author(s): Aug 28, 2019

Reporting Summary

Nature Research wishes to improve the reproducibility of the work that we publish. This form provides structure for consistency and transparency in reporting. For further information on Nature Research policies, see Authors & Referees and the Editorial Policy Checklist.

Statistics

For all statistical analyses, confirm that the following items are present in the figure legend, table legend, main text, or Methods section.

n/a	Confirmed
☐	☒ The exact sample size (*n*) for each experimental group/condition, given as a discrete number and unit of measurement
☐	☒ A statement on whether measurements were taken from distinct samples or whether the same sample was measured repeatedly
☒	☐ The statistical test(s) used AND whether they are one- or two-sided *Only common tests should be described solely by name; describe more complex techniques in the Methods section.*
☒	☐ A description of all covariates tested
☒	☐ A description of any assumptions or corrections, such as tests of normality and adjustment for multiple comparisons
☒	☐ A full description of the statistical parameters including central tendency (e.g. means) or other basic estimates (e.g. regression coefficient) AND variation (e.g. standard deviation) or associated estimates of uncertainty (e.g. confidence intervals)
☒	☐ For null hypothesis testing, the test statistic (e.g. *F*, *t*, *r*) with confidence intervals, effect sizes, degrees of freedom and *P* value noted *Give P values as exact values whenever suitable.*
☒	☐ For Bayesian analysis, information on the choice of priors and Markov chain Monte Carlo settings
☒	☐ For hierarchical and complex designs, identification of the appropriate level for tests and full reporting of outcomes
☒	☐ Estimates of effect sizes (e.g. Cohen's *d*, Pearson's *r*), indicating how they were calculated

Our web collection on statistics for biologists contains articles on many of the points above.

Software and code

Policy information about availability of computer code

Data collection	Cryo-EM images were collected using SerialEM (http://bio3d.colorado.edu/SerialEM/).
Data analysis	Motion correction was done using MotionCor2 (https://emcore.ucsf.edu/ucsf-motioncor2) CTF parameters were estimated by Gctf (https://www.mrc-lmb.cam.ac.uk/kzhang/Gctf/). 2D and 3D classification, 3D refinement were done using Relion 2.0 and 3.0 (https://www3.mrc-lmb.cam.ac.uk/relion/index.php/Main_Page). Local resolution map was computed by ResMap-1.1.4 (https://github.com/akucukelbir/resmap). Model fitting and building were done using UCSF Chimera-1.11.2 (https://www.cgl.ucsf.edu/chimera/) and Coot-0.8.7 (https://www2.mrc-lmb.cam.ac.uk/personal/pemsley/coot/), respectively. Model refinement was done using Phenix-1.14 (https://www.phenix-online.org/).

For manuscripts utilizing custom algorithms or software that are central to the research but not yet described in published literature, software must be made available to editors/reviewers. We strongly encourage code deposition in a community repository (e.g. GitHub). See the Nature Research guidelines for submitting code & software for further information.

Data

Policy information about availability of data

All manuscripts must include a data availability statement. This statement should provide the following information, where applicable:

- Accession codes, unique identifiers, or web links for publicly available datasets
- A list of figures that have associated raw data
- A description of any restrictions on data availability

Atomic coordinates have been deposited in the Protein Data Bank (PDB) under the accession code 6K61. The cryo-EM density map has been uploaded to the Electron Microscopy Data Bank (EMDB) under the accession code EMD-9918.

Field-specific reporting

Please select the one below that is the best fit for your research. If you are not sure, read the appropriate sections before making your selection.

☒ Life sciences ☐ Behavioural & social sciences ☐ Ecological, evolutionary & environmental sciences

For a reference copy of the document with all sections, see nature.com/documents/nr-reporting-summary-flat.pdf

Life sciences study design

All studies must disclose on these points even when the disclosure is negative.

Sample size	No statistic method was used to predetermine the sample size. The number of particles used in structural determination was not pre-determined, and the results indicated that the size is sufficient to generate a density map at 2.37 A resolution.
Data exclusions	Regarding the cryo-EM raw micrograph screening, exclusion was done based on the quality of the images and the presence of ice contamination. Regarding the particle selection, 2D and 3D classification were used and criterion is based on the quality of resulting 2D class average and 3D maps.
Replication	Multiple rounds of structural refinement have been performed and all resulted in same density maps (with different resolutions though). For functional measurement, at least three replications were done to calculated the means and S.D.
Randomization	No randomization was used, because our study focused on a specific protein complex.
Blinding	No blinding in structural and functional data analysis. Binding is not relevant, as we are studying a specific protein complex.

Reporting for specific materials, systems and methods

We require information from authors about some types of materials, experimental systems and methods used in many studies. Here, indicate whether each material, system or method listed is relevant to your study. If you are not sure if a list item applies to your research, read the appropriate section before selecting a response.

Materials & experimental systems

n/a	Involved in the study
☐	☒ Antibodies
☒	☐ Eukaryotic cell lines
☒	☐ Palaeontology
☒	☐ Animals and other organisms
☒	☐ Human research participants
☒	☐ Clinical data

Methods

n/a	Involved in the study
☒	☐ ChIP-seq
☒	☐ Flow cytometry
☒	☐ MRI-based neuroimaging

Antibodies

Antibodies used	Primary antibody of rabbit anti-NifH was made on house (described in the legend of Supplementary Fig. 10). Secondary antibody HRP-IgG (goat, anti-rabbit IgG, Biodragon Immunotechnologies, Cat#BF03008) .
Validation	Information of the secondary antibody validation is available through manufacturer's online database (https://www.biomart.cn/infosupply/33612185.htm). The primary antibody was generated previously and has been validated by immunoblotting several time.